

■ Past endolithic life in metamorphic ocean crust

X. Peng, Z. Guo, M. Du, A.D. Czaja, D. Papineau, S. Chen,
H. Xu, J. Li, K. Ta, S. Bai, S. Dasgupta

■ Supplementary Information

The Supplementary Information includes:

- Materials and Methods
- Supplementary Text
- Tables S-1 to S-4
- Figures S-1 to S-9
- Video S-1
- Supplementary Information References

Materials and Methods

Sampling

The low-grade metamorphic rocks that have been tectonically extruded at the seafloor were recovered from the southern Mariana trench (SMT) (Table S-1), using manipulators of the manned submersible *Jiaolong* during two cruises of R/V XYH09 from June to July 2016 and from May to June 2017. After recovery, the rock samples were immediately placed in a biobox equipped on submersible *Jiaolong* to avoid potential contamination from seawater. Sediments were collected with push-core samplers. Once on deck, metamorphic rocks and sediment samples were immediately subsampled and stored at -20 °C or -80 °C until further analysis.

X-ray diffraction analysis

Mineral compositions were determined using Cu K α radiation on a Bruker D8 Advance X-ray diffractometer, which was operated at 40 kV and 40 mA with a scanning speed of 2°/min between 3° and 70° at Guangzhou Institute of Geochemistry, Chinese Academy of Sciences. Prior to X-ray diffraction (XRD) analysis, small pieces of the analysed metamorphic rocks were ultrasonicated in deionised water, freeze-dried under anoxic conditions to avoid oxidation during drying and then thoroughly ground using a pestle and mortar.

Scanning electron microscopy

Back-scattered electron (BSE) images of rock chips were collected using a FEI Quanta FEG 250 high-resolution field emission



scanning electron microscopy (SEM) equipped with an EDAX energy dispersive X-ray spectroscopy (EDS) analysis system at FEI Trading (Shanghai) Co. Ltd (China). SEM was operated at 5 or 10 kV with a working distance of 10 mm to provide optimal imaging and minimise charging and sample damage in the BSE imaging mode. An accelerating voltage of 20 kV was used for the X-ray analysis to acquire elemental distributions.

Nano-scale secondary ion mass spectrometry

Elemental maps were performed on the polished 30- μm -thick thin sections using a Cameca NanoSIMS 50L (CAMECA, Paris, France) at the Institute of Geology and Geophysics, Chinese Academy of Sciences, following the procedure previously described (Peng *et al.*, 2016). Each region of interest was pre-sputtered with a 150 pA beam current and an ion dose of $N = 5 \times 10^{16}$ ions/cm² to remove the conductive coating (Au) and the contaminants that were generated during pretreatment. In the multi-collection mode, negative secondary ions (¹²C⁻, ¹²C¹⁴N⁻, ²⁸Si⁻, ³¹P⁻, ³²S⁻, ²⁴Mg¹⁶O⁻, and ⁵⁶Fe¹⁶O⁻) were sputtered from the sample surface using a Cs⁺ primary beam with ~ 2.5 pA intensity. All of the images referred to in this paper are 256 \times 256 pixels, recorded in ~ 30 min.

Raman spectrometry

Rock chips were analysed using a LabRAM HR Evolution (Horiba Jobin Yvon) confocal Raman spectrometer equipped with a 532 nm excitation laser at the Institute of Deep-sea Science and Engineering, Chinese Academy of Sciences. Individual spectra were recorded using 50 \times objective lens, ~ 1 μm diameter analysing spot area, ~ 3 mW laser power, and 10 s \times 2 measuring sequence. The analytical methods were described elsewhere (Guo *et al.*, 2018). Micro-Raman imaging was performed primarily on polished thin sections with the a300 WITec confocal laser scanning micro-spectroscopy system at the University College of London (UCL), using a 532 nm laser tuned at 12 mW coupled to an inverted optical microscope by an optical fiber, according to previously described techniques (Papineau *et al.*, 2017). In brief, a 50 microns diameter optic fiber is used to harvest the inelastically scattered photons. A 100 \times objective is used to provide a spatial resolution between 500 and 360 nm in the Raman images, whereas a 600 lines/mm grating is used to obtain spectra with a spectral resolution around 4 cm⁻¹. Raman hyperspectral images of mineral associations were generated by mapping the main peak intensities for specific minerals using the WITec Project Four Plus data processing software; the peaks include those distinct for quartz (~ 467 cm⁻¹), feldspar (~ 509 cm⁻¹), celadonite (~ 620 cm⁻¹), and carbonaceous matter (~ 1576 cm⁻¹). All Raman peak positions were read directly from measured average spectra calculated from representative regions with high signal-to noise and after background removal.

Confocal laser scanning microscopy

Microfossil structures were located and photographed within the polished thin sections using a Leica DM2700P polarising light microscopy in transmitted white light with a wavelength of 550 nm. Two- and three-dimensional fluorescence images of selected specimens were acquired with an Olympus Fluoview 1200 confocal laser scanning microscopy (CLSM; Olympus, Inc., Shinjuku, Japan) running the FV10-ASW software (v. 3.01) at the University of Cincinnati, following the procedure previously described (Guo *et al.*, 2018). No stains were used on the samples because the filamentous structures of interest are embedded in a mineral matrix, and thus, the CLSM images are based on autofluorescence. The CLSM was operated at 488 nm laser excitation, a 60 \times oil-immersion objective (NA [numerical aperture] = 1.42) with fluorescence-free microscopy immersion oil (Olympus Type-F), and a 505-605 nm bandpass filter to exclude the incident laser wavelength. The 2-D images were exported as TIF files and then rendered into 3-D images by use of the software program Paraview v. 5.0.1 (Kitware Inc., Clifton Park, NY).

Carbon and oxygen isotope compositions

Analyses of carbon and oxygen isotope compositions were carried out from bulk rock powders and surrounding sediments at the



Stable Isotope Laboratory, Third Institute of Oceanography, State Oceanic Administration, China. Total inorganic carbon (TIC) was determined using Gas Bench II–IRMS by extracting CO₂ from ~100 µg of powdered sample treated with 100% orthophosphoric acid. Total organic carbon (TOC) was determined using Element Analyzer (Flash EA 1112 HT) after removing carbonate. Total carbon (TC) was calculated by adding TIC and TOC. Reproducibility for TIC and TOC were approximately 0.3 %. The δ¹³C_{TOC}, δ¹³C_{TIC} and δ¹⁸O_{CaCO₃} values were analysed using the stable isotope mass spectrometer (Thermo Delta V Advantages). Carbon isotope values are reported as standard δ-notation (in units of per mil, ‰), relative to the Vienna Pee Dee Belemnite (VPDB) standard. They were calculated according to the following equation:

$$\delta^{13}\text{C} (\text{‰}) = [({}^{13}\text{C}/{}^{12}\text{C})_{\text{sample}} / ({}^{13}\text{C}/{}^{12}\text{C})_{\text{VPDB}} - 1] \times 1000 \quad \text{Eq. S-1}$$

where ({}¹³C/{}¹²C)_{VPDB} is the carbon isotope ratio of VPDB. The analytical accuracy of the δ¹³C values was better than ±0.2‰.

Oxygen isotope values are reported as standard δ-notation (in units of per mil, ‰), relative to the SMOW standard. They were calculated according to the following equation:

$$\delta^{18}\text{O} (\text{‰}) = [({}^{18}\text{O}/{}^{16}\text{O})_{\text{sample}} / ({}^{18}\text{O}/{}^{16}\text{O})_{\text{SMOW}} - 1] \times 1000 \quad \text{Eq. S-2}$$

where ({}¹⁸O/{}¹⁶O)_{SMOW} is the oxygen isotope ratio of SMOW. The analytical accuracy of the δ¹⁸O values was better than ±0.2‰.

Staining

Thin sections were stained with the 4, 6-diamidino-2-phenylindole (DAPI) stain and examined by epifluorescence microscopy, following the procedure previously described (Fisk *et al.*, 2006). The petrographic thin section was rinsed with 10 ml of 75 % (vol/vol) ethanol, air-dried in a clean hood for 5 min, and then submerged in a 1:500 dilution of filter-sterilised (0.2 µm pore size) 0.1% (wt/vol) DAPI, which was dissolved in autoclaved phosphate-buffered saline solution (PBS; pH adjusted to 7.4). The petrographic thin section was subsequently subjected to the pressure from 1 atmosphere to partial vacuum (3.3 kPa for 2 min) after which the sample was incubated with the dye at 37 °C for 0.5 h. Following incubation, the thin section was rinsed with repeated washes of 50 ml of filter-sterilised PBS buffer. To remove unbound stain, the thin section was also cycled to partial vacuum and back to atmospheric pressure during washing. The thin section was imaged using an epifluorescence microscopy (Leica DM6B), which was operated at filter system for blue excitation with a 450-490 nm excitation filter, a 510 nm dichromatic mirror, and a 515 nm suppression filter.

Lipid analysis

The selected rocks were divided carefully into the inner and outer portions using a sterilised scoop cleaned with dichloromethane (Fig. S-9). Then, rock and sediment samples were grounded into powder using an agate pestle and mortar after freeze-drying. Approximately 15 g of the powder was extracted ultrasonically with a mixture of methanol (MeOH), dichloromethane and phosphate buffer at pH 7.4 (1:1:0.8, v/v, ×4) using a modified Bligh and Dyer method (Sturt *et al.*, 2004). After separation into an organic phase and an aqueous phase by centrifugation at 2500 rpm for 10 min, the bottom dichloromethane phase was collected using a glass pipette (×3), dried under a stream of nitrogen gas and then redissolved in 500 µl of hexane : dichloromethane 70:30 mixture.

Total lipids were separated into hydrocarbons, neutral lipids, and phospholipids using miniature silicic acid columns (Supelco Inc., Bellefonte, Pennsylvania, U.S.A.) eluted sequentially with 5 ml of hexane, chloroform, and methanol, respectively. The hydrocarbon (HC) fraction was dried in a gentle stream of nitrogen and resuspended in dichloromethane for GC-MS analysis. The neutral lipid (NL) fractions were dried under a stream of nitrogen, derivatised by adding 60 µl of N, O-bis (trimethylsilyl)-trifluoroacetamide, and heated at 65°C for 40 min to produce trimethylsilyl ethers of sterols and alcohols (Fang *et al.*, 2007). 5α-



cholestane was used as an internal standard for quantification. Phospholipid fraction was subjected to a mild alkaline trans-methylation procedure to produce fatty acid methyl esters (FAME) (Fang *et al.*, 1996).

All the lipids were analysed on an Agilent 6890 Gas Chromatograph (GC) interfaced with an Agilent 5973 N Mass Selective Detector. Analytical separation of lipids was accomplished using a 30 m × 0.25 mm (internal diameter) DB-5 fused-silica capillary column (J&W Scientific, Folsom, California, U.S.A.). Column temperature was programmed from 50 to 120 °C at 10 °C min⁻¹, then to 310 °C at 5 °C min⁻¹, and held at 310 °C for 20 min. Lipids were identified based on mass spectra. Concentrations of lipids were obtained based on the gas chromatograph-mass spectrometer (GC-MS) response relative to that of an internal standard—C18 fatty acid ethyl ester for fatty acids and 5 α -cholestane for hydrocarbons and neutral lipids. However, lipid biomarker (HC, NL, FAME) failed to be detected in our samples.

For analysis of glycerol dialkyl glycerol tetraether (GDGTs), C₄₆ GDGT was added as internal standard to a part of the total lipid extract, dried under a stream of nitrogen gas, dissolved in hexane/isopropanol (99:1, v/v) and then passed through 0.45- μ m polytetrafluoroethylene filters.

The GDGTs were analysed using an Agilent 1200 high performance liquid chromatography (HPLC) device connected to an Agilent 6460 triple quadrupole mass spectrometer, following the procedure described in Xie *et al.* (2015). The GDGT compounds were separated using an Alltech Prevail Cyano column (150 mm × 2.1 mm, 3 μ m) at 30°C. The injection volume was 10 μ l. For the first 5 min, GDGTs were eluted isocratically with n-hexane/isopropanol (99:1, v/v), followed by a linear gradient to 1.8% hexane/isopropanol (90:10, v/v) in 45 min. The flow rate was maintained at 0.2 ml/min. The column was cleaned by back flushing hexane/propanol (90:10, v/v) at 0.2 ml/min for 10 min after each analysis. The GDGTs (m/z 1302, 1300, 1298, 1296, 1294, 1292, 1018, 1020, 1022, 1032, 1034, 1036, 1046, 1048 and 1050) and C₄₆ GDGT internal standard (m/z 744) were quantified by integration of peak areas from the extracted ion chromatograms.

The GDGTs membrane lipids of prokaryotes include archaeal isoprenoidal GDGTs (IsoGDGTs) and bacterial branched GDGTs (BrGDGTs). They have been widely used for tracing the sources of organic matter due to the difference in BrGDGTs and IsoGDGTs (Schouten *et al.*, 2013; Weijers *et al.*, 2014). Based on BrGDGTs and crenarchaeol (representative of marine IsoGDGTs) membrane lipids, the branched vs. isoprenoid tetraether (BIT) index was calculated following the equation of Hopmans *et al.* (2004):

$$\text{BIT index} = \frac{\text{GDGT I} + \text{GDGT II} + \text{GDGT III}}{\text{GDGT I} + \text{GDGT II} + \text{GDGT III} + \text{Crenarchaeol}} \quad \text{Eq. S-3}$$

Ammonium contents

Ammonium was extracted using the HF digestion and distillation technique, following the procedure previously described (Hall, 1993). Approximately 200–300 mg of the dried sample powders were weighed into PTFE bottles and then digested using 2 ml of 40% HF. The duration of the digestion was at least 7 days at room temperature, with the samples gently shaken on a regular basis. After digestion, about 20 ml of 25 % KOH solution was added to raise the pH, and the whole solution was distilled using a Kjeldahl apparatus until 15 ml of distillate had been collected in a 15 ml 0.01 N HCl solution. The amount of NH₄⁺ was determined by colorimetry with phenol and sodium hypochlorite. Each sample was digested and analysed in triplicate, with a relative error of less than 10%.

Thermodynamic calculations

The amount of metabolic energy that is potentially available to a microorganism from a chemical reaction are calculated using the equation



$$\Delta G = \Delta G^\circ + RT \ln Q \quad \text{Eq. S-4}$$

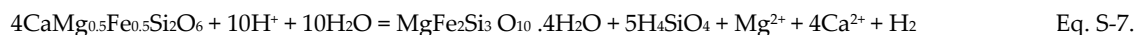
where ΔG° represents the standard free energy, ΔG is the free energy, T is the temperature in Kelvin, and R is the universal gas constant, and Q stands for the activity product of the species involved in the reaction. Autotrophic hydrogen oxidation proceeds according to the reaction



Autotrophic ammonium oxidation proceeds according to the reaction



We assume that H_2 is generated through the alteration of pyroxene that accounts for 59 % of basaltic rocks. H_2 generation in pyroxene is calculated according to the equation:



NH_4^+ contents in metamorphic rocks are used to calculate the amount of energy by autotrophic ammonium oxidation. It is also assumed that chemolithoautotrophs require 292 kJ to fix 1 g of biomass.

Supplementary Text

Frutexitis-like structures

These arborescent structures branch off from main stems and have rounded terminations. Micro-Raman mapping shows that they contain μm -scale quartz, feldspar, celadonite and carbonaceous matter (Fig. 2l). Carbonaceous matter commonly occur as bulbous filaments that branch and vary from several hundreds of microns to up to 5 millimeters in length. Small carbonaceous grains also form discontinuous trails and disseminations on the surroundings of the *Frutexitis*-like structures (Fig. 2k,l). These biogenic structures are distinctly different from abiogenic dendrites of Mn-oxide (Xu *et al.*, 2010) because they contain abundant carbonaceous matter and no Mn detected by SEM-EDS.

Lipid biomarkers

To further demonstrate the *in situ* production of organic carbon, we conducted lipid analyses of the inner and outer portions of metamorphic rocks. Only tetraether lipids were detected (Table S-3); no hydrocarbons, neutral lipids or fatty acid methyl esters were detected in these metamorphic rocks. Because the latter are common in seawater, this indicates that potential seawater or any other form of contamination was minimal.

Bioenergetic calculations

We use bioenergetic calculations based on redox reactions between H_2 and CO_2 , as well as NH_4^+ and NO_3^- , to provide preliminary estimates of the potential energy that is available for *in situ* biomass production within low-grade metamorphic crust. Despite the existence of uncertainties, these calculations indicate the energy yielded by the reactions in 1 g metamorphic rock might support the production of 2.18×10^{-4} g of biomass associated with methanotrophy and 6.69×10^{-7} g of biomass associated with anaerobic ammonium oxidation, the total of which falls within the range of TOC content (0.008 wt. % to 0.379 wt. %) of metamorphic rocks.

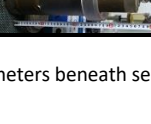


Supplementary Tables

Table S-1 Location information and mineralogy characterisation of the metamorphic rocks and surrounding sediments in the subduction zone of the SMT.

| Sample ID | Samples | Depth (mbsla) | Latitude N | Longitude E | Sample methods | Mineral composition |
|-----------|---|---------------|------------|-------------|----------------|--|
| JL118-G03 |  | 6695 | 11.580° | 141.883° | Jiaolong dive | Analcite, Chabazite, feldspar, chlorite |
| JL118-G04 |  | 6692 | 11.581° | 141.882° | Jiaolong dive | Heulandite, mordenite, gismondine, maghemite |
| JL118-G06 |  | 6694 | 11.581° | 141.882° | Jiaolong dive | Analcite, gmelinite, chabazite |
| JL119-G01 |  | 5997 | 11.665 | 142.250 | Jiaolong dive | Phillipsite, plagioclase, gmelinite, illite, quartz, maghemite |
| JL119-G02 |  | 6001 | 11.665° | 142.249° | Jiaolong dive | Phillipsite, plagioclase, gmelinite, maghemite |
| JL120-G01 |  | 6706 | 11.583° | 141.878° | Jiaolong dive | Analcite, phillipsite, gmelinite, hematite |
| JL120-G02 |  | 6702 | 11.583° | 141.878° | Jiaolong dive | Analcite, phillipsite, gmelinite, talc, hematite |
| JL120-G03 |  | 6705 | 11.583° | 141.878° | Jiaolong dive | Heulandite/clinoptilolite, magnetite |
| JL121-G01 |  | 5590 | 11.799° | 142.113° | Jiaolong dive | Phillipsite, plagioclase, quartz, maghemite |
| JL121-G04 |  | 5552 | 11.800° | 142.116° | Jiaolong dive | Phillipsite, Labradorite, chlorite, quartz, maghemite |
| JL122-G01 |  | 6296 | 10.890° | 142.227° | Jiaolong dive | Celadonite, ilmenite |
| JL122-G02 |  | 6296 | 10.890° | 142.227° | Jiaolong dive | Celadonite, augite, ilmenite |
| JL144-G03 |  | 6304 | 10.889° | 142.227° | Jiaolong dive | Natrolite, maghemite, labradorite, augite |
| JL145-G02 |  | 6531 | 11.630° | 142.144° | Jiaolong dive | Phillipsite, natrolite, ferripyrophyllite |



| | | | | | | |
|-----------|---|------|---------|----------|-------------------|--|
| JL146-G01 |  | 6697 | 10.920° | 141.696° | Jiaolong dive | Phillipsite, gmelinite, labradorite, maghemite |
| JL146-G02 |  | 6685 | 10.920° | 141.696° | Jiaolong dive | Phillipsite, gmelinite, labradorite, maghemite |
| JL146-G05 |  | 6406 | 10.909° | 141.704° | Jiaolong dive | Phillipsite, muscovite, labradorite, clinochlore, ferrihydrite |
| JL147-G03 |  | 6684 | 10.961° | 141.983° | Jiaolong dive | Phillipsite, gmelinite, labradorite, chlorite |
| JL147-G06 |  | 6053 | 10.957° | 141.986° | Jiaolong dive | Phillipsite, natrolite, plagioclase, clinochlore |
| JL147-G07 |  | 6053 | 10.957° | 141.986° | Jiaolong dive | Phillipsite, muscovite, plagioclase, clinochlore, maghemite |
| JL147-G08 |  | 6053 | 10.957° | 141.986° | Jiaolong dive | Natrolite, plagioclase, augite, maghemite |
| JL147-G10 |  | 6053 | 10.957° | 141.986° | Jiaolong dive | Natrolite, labradorite, augite, magnetite |
| JL120-S01 |  | 6707 | 11.582° | 141.879° | Push-core sampler | Analcite, plagioclase, quartz, clinochlore |
| JL121-S01 |  | 5569 | 11.800° | 142.115° | Push-core sampler | Gismondine, plagioclase, quartz, clinochlore |
| JL122-S01 |  | 6329 | 10.889° | 142.228° | Push-core sampler | Phillipsite, muscovite, plagioclase, quartz, clinochlore |

^a mbsl means meters beneath sea level.



Table S-2 Geochemical characterisation of the metamorphic rocks in the subduction zone of the SMT.

| Sample ID | TOC ^a (wt. %) | TIC ^b (wt. %) | TC ^c (wt. %) | $\delta^{13}\text{C}_{\text{TOC}}$ (‰VPDB) | $\delta^{13}\text{C}_{\text{TIC}}$ (‰VPDB) | $\delta^{18}\text{O}$ ^d (‰SMOW) | Temperature ^e (°C; -4‰ fluid) |
|-----------|--------------------------|--------------------------|-------------------------|--|--|---|---|
| JL118-G03 | 0.013 | 0.012 | 0.025 | -23.7 | -6.1 | 25.3 | 20 |
| JL118-G04 | 0.008 | 0.004 | 0.012 | -25.9 | -9.9 | 20.4 | 44 |
| JL118-G06 | 0.011 | 0.011 | 0.022 | -24.7 | -7.5 | 21.8 | 36 |
| JL119-G01 | 0.046 | 0.014 | 0.060 | -22.5 | -10.6 | 14.0 | 88 |
| JL119-G02 | 0.016 | 0.007 | 0.023 | -25.9 | -11.7 | 14.2 | 86 |
| JL120-G01 | 0.013 | 0.006 | 0.020 | -25.0 | -7.3 | 21.3 | 39 |
| JL120-G02 | 0.018 | 0.006 | 0.023 | -24.6 | -7.0 | 24.3 | 24 |
| JL120-G03 | 0.013 | 0.009 | 0.022 | -24.7 | -12.9 | 14.0 | 89 |
| JL121-G01 | 0.026 | 0.007 | 0.032 | -23.0 | -11.3 | 14.7 | 82 |
| JL121-G04 | 0.034 | 0.08 | 0.042 | -22.4 | -12.3 | 14.0 | 88 |
| JL122-G01 | 0.020 | 0.005 | 0.025 | -26.2 | -9.3 | 20.6 | 43 |
| JL122-G02 | 0.013 | 0.005 | 0.018 | -24.9 | -11.6 | 13.9 | 89 |
| JL144-G03 | 0.090 | 0.031 | 0.122 | -25.2 | -8.2 | - | - |
| JL145-G02 | 0.261 | 0.141 | 0.402 | -26.0 | -13.0 | - | - |
| JL146-G01 | 0.296 | 0.116 | 0.411 | -26.5 | -13.9 | - | - |
| JL146-G02 | 0.379 | 0.039 | 0.418 | -25.2 | -13.8 | - | - |
| JL146-G05 | 0.025 | 0.104 | 0.129 | -25.3 | -14.5 | - | - |
| JL147-G03 | 0.032 | 0.114 | 0.147 | -25.4 | -12.8 | - | - |
| JL147-G06 | 0.037 | 0.067 | 0.104 | -23.2 | -13.1 | - | - |
| JL147-G07 | 0.032 | 0.075 | 0.107 | -26.1 | -11.1 | - | - |
| JL147-G08 | 0.010 | 0.043 | 0.053 | -28.8 | -6.8 | - | - |
| JL147-G10 | 0.013 | 0.054 | 0.067 | -29.5 | -9.7 | - | - |
| Average | 0.064 | 0.040 | 0.104 | -25.2 | -10.7 | 18.2 | 61 |

^a Total organic carbon.^b Total inorganic carbon.^c Total carbon calculated by adding TIC and TOC.^d Oxygen isotope composition of carbonates extracted from metamorphic rocks.^e The temperature was estimated by the algebraic equation described previously:

$$1000\ln a = 2.78 \times (10^6 T^{-2}) - 3.39$$

where the fractionation factor $a = (^{18}\text{O}/^{16}\text{O})_{\text{CaCO}_3} / (^{18}\text{O}/^{16}\text{O})_{\text{fluid}}$, and we assumed equilibrium with ^{18}O -depleted fluids (-4 ‰, SMOW) resulted from low-temperature reaction of seawater with basalt (Alt *et al.*, 1986).



Table S-3 The GDGTs concentrations (ng/g extract) of metamorphic rocks and sediments from the SMT.

| Sample ID | | GDGT-0 | GDGT-1 | GDGT-2 | GDGT-3 | Crenarchaeol | br-GDGT-III | br-GDGT-IIIb | br-GDGT-IIIc | br-GDGT-II | br-GDGT-IIb | br-GDGT-IIc | br-GDGT-I | br-GDGT-Ib | br-GDGT-Ic | ΣBr-GDGT | BIT |
|---------------------|-----------|--------|--------|--------|--------|--------------|-------------|--------------|--------------|------------|-------------|-------------|-----------|------------|------------|----------|------|
| | | 1302 | 1300 | 1298 | 1296 | 1292 | 1050 | 1048 | 1046 | 1036 | 1034 | 1032 | 1022 | 1020 | 1018 | | |
| JL121-G04-1 (Inner) | rocks | 0.195 | 0.011 | 0.007 | 0.001 | 0.135 | 0.247 | 0.024 | 0.018 | 0.103 | 0.014 | 0.007 | 0.053 | 0.013 | 0.004 | 0.483 | 0.75 |
| JL121-G04-2 (Outer) | rocks | 5.445 | 0.154 | 2.107 | 0.120 | 14.527 | 1.621 | 0.017 | 0.016 | 0.298 | 0.033 | 0.000 | 0.414 | 0.050 | 0.023 | 2.471 | 0.14 |
| JL120-G02 (Inner) | rocks | 0.086 | 0.004 | 0.003 | 0.000 | 0.047 | 0.017 | 0.004 | 0.000 | 0.009 | 0.003 | 0.000 | 0.009 | 0.002 | 0.002 | 0.044 | 0.42 |
| JL121-G01 (Inner-1) | rocks | 0.693 | 0.439 | 0.526 | 0.019 | 0.012 | 0.239 | 0.032 | 0.148 | 0.021 | 0.000 | 0.000 | 0.131 | 0.005 | 0.004 | 0.581 | 0.97 |
| JL121-G01 (Inner-2) | rocks | 0.800 | 0.011 | 0.005 | 0.002 | 0.192 | 0.355 | 0.000 | 0.000 | 0.157 | 0.000 | 0.000 | 0.085 | 0.000 | 0.000 | 0.597 | 0.76 |
| JL122-G02-1 (Inner) | rocks | 0.297 | 0.009 | 0.004 | 0.001 | 0.081 | 0.126 | 0.006 | 0.004 | 0.048 | 0.006 | 0.000 | 0.035 | 0.000 | 0.000 | 0.225 | 0.72 |
| JL122-G02-2 (Outer) | rocks | 8.784 | 2.123 | 2.735 | 0.147 | 17.427 | 2.507 | 0.016 | 0.018 | 0.415 | 0.027 | 0.017 | 0.455 | 0.056 | 0.025 | 3.538 | 0.16 |
| JL121 0-2 | sediments | 6.478 | 1.914 | 2.296 | 0.153 | 13.846 | 1.429 | 0.038 | 0.024 | 0.283 | 0.048 | 0.016 | 0.274 | 0.059 | 0.026 | 2.196 | 0.13 |
| JL121 11-12 | sediments | 11.385 | 3.136 | 4.649 | 0.310 | 22.633 | 3.787 | 0.100 | 0.049 | 0.694 | 0.105 | 0.039 | 0.792 | 0.139 | 0.057 | 5.762 | 0.19 |
| JL122 15-16 | sediments | 5.317 | 1.632 | 2.316 | 0.137 | 12.653 | 2.115 | 0.039 | 0.018 | 0.469 | 0.113 | 0.036 | 0.493 | 0.070 | 0.028 | 3.381 | 0.20 |
| JL120 23-24 | sediments | 11.035 | 3.108 | 4.578 | 0.320 | 26.826 | 3.080 | 0.044 | 0.031 | 0.595 | 0.075 | 0.033 | 0.760 | 0.113 | 0.051 | 4.784 | 0.14 |
| JL120 11-12 | sediments | 5.082 | 1.292 | 1.524 | 0.436 | 10.783 | 1.952 | 0.029 | 0.020 | 0.371 | 0.037 | 0.017 | 0.474 | 0.070 | 0.031 | 2.999 | 0.21 |
| JL114 0-2 | sediments | 4.939 | 1.253 | 2.015 | 0.718 | 18.835 | 4.453 | 0.132 | 0.133 | 1.160 | 0.153 | 0.074 | 1.236 | 0.182 | 0.143 | 7.665 | 0.27 |
| Blank-1 | | 0 | 0 | 0 | 0 | 0 | 0 | 0 | 0 | 0 | 0 | 0 | 0 | 0 | 0 | 0 | |
| Blank-2 | | 0 | 0 | 0 | 0 | 0 | 0 | 0 | 0 | 0 | 0 | 0 | 0 | 0 | 0 | 0 | |



Table S-4 Comparison of ammonium (NH_4^+) contents in basalts and metamorphic rocks

| Rock type | Sample ID | NH_4^+ contents (ppm) |
|-------------------|-----------|--------------------------------|
| Basalts | JL116-G02 | 0.78 |
| | JL116-G04 | 1.35 |
| Metamorphic rocks | JL120-G01 | 7.49 |
| | JL122-G01 | 7.16 |
| | JL122-G02 | 11.82 |



Supplementary Figures

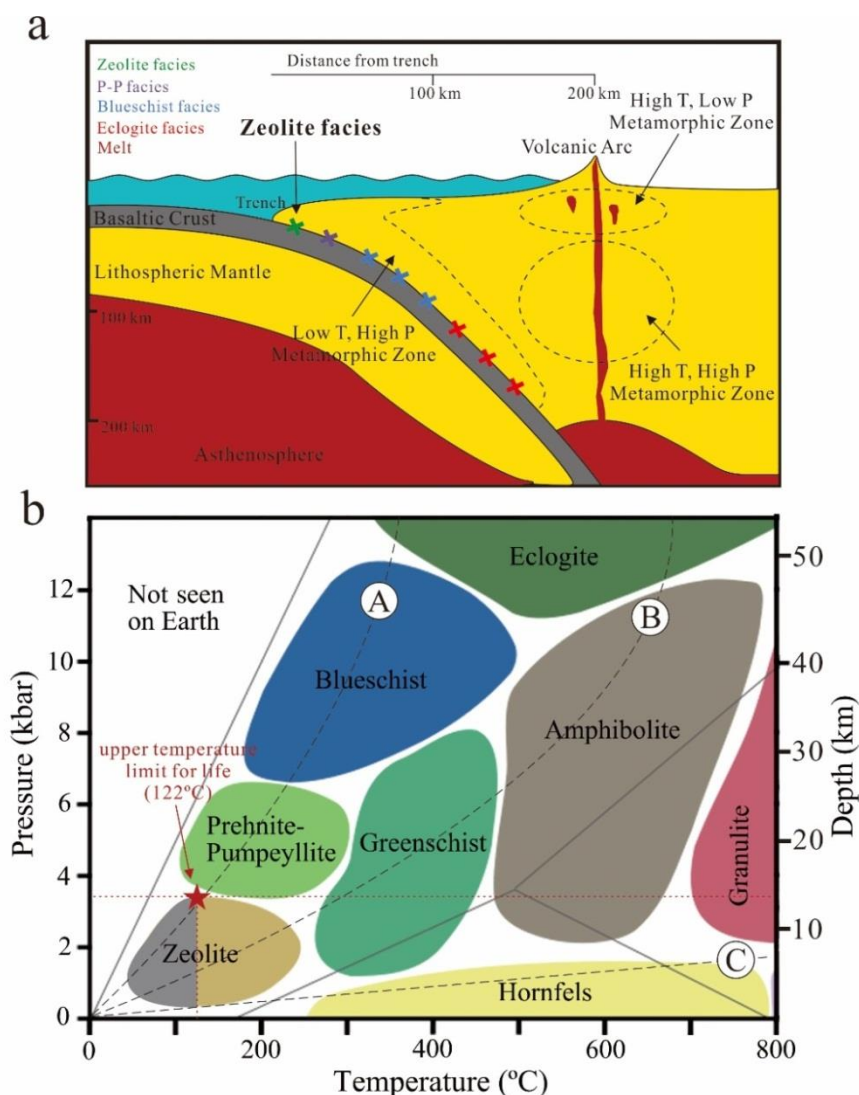


Figure S-1 Representative metamorphic zones and facies diagram. **(a)** Metamorphic zones near plate margins (modified from Winter, 2010), showing subduction zone metamorphism is characterised by a metamorphic path through zeolite, prehnite-pumpellyite (P-P), blueschist, and eclogite facies stability zones of subducted oceanic crust. **(b)** Metamorphic facies in pressure-temperature (P-T) diagram (modified from Marshak, 2009). Curve A represents a low geothermal gradient (Low T, High P), such as subduction zone metamorphism. Curve B represents a normal geothermal gradient (High T, High P), such as regional metamorphism. Curve C represents a high geothermal gradient (High T, Low P), such as contact metamorphism. Note that zeolite-facies rocks are first metamorphosed from basaltic rocks at depths of 1-14 km beneath the seafloor and temperatures of approximately 40-300 °C, part of which is well within the tolerance of life (<122 °C), as indicated by grey area.



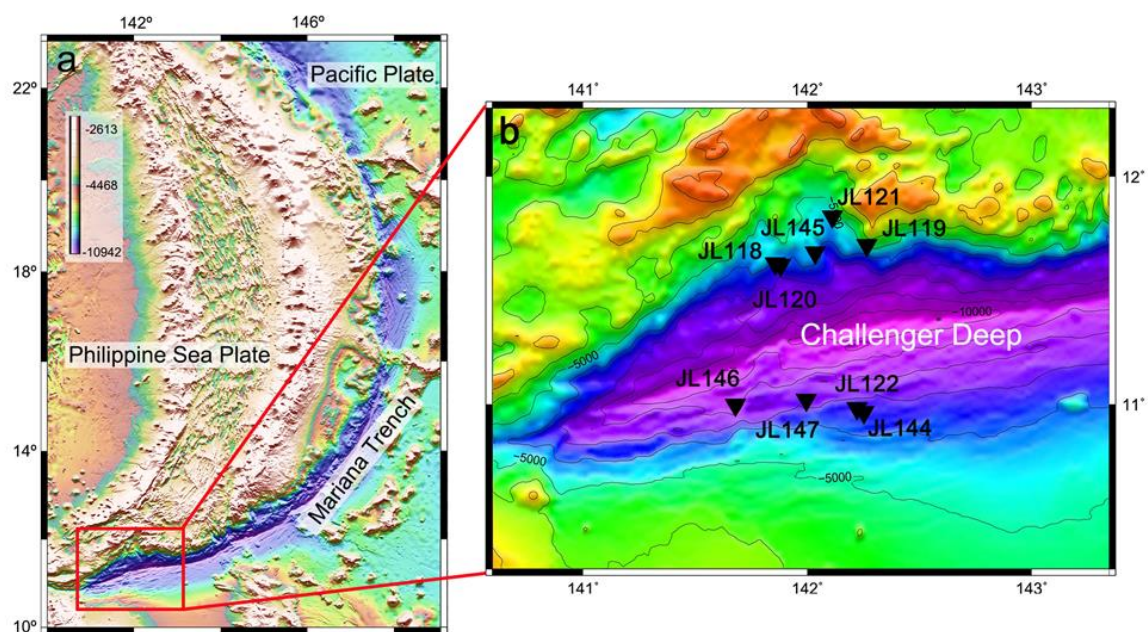


Figure S-2 (a) Color bathymetry map of the Philippine Sea region of the western Pacific displaying the location of the SMT (red box). **(b)** Enlarged map of the SMT with Jiaolong dive sites (black triangles).

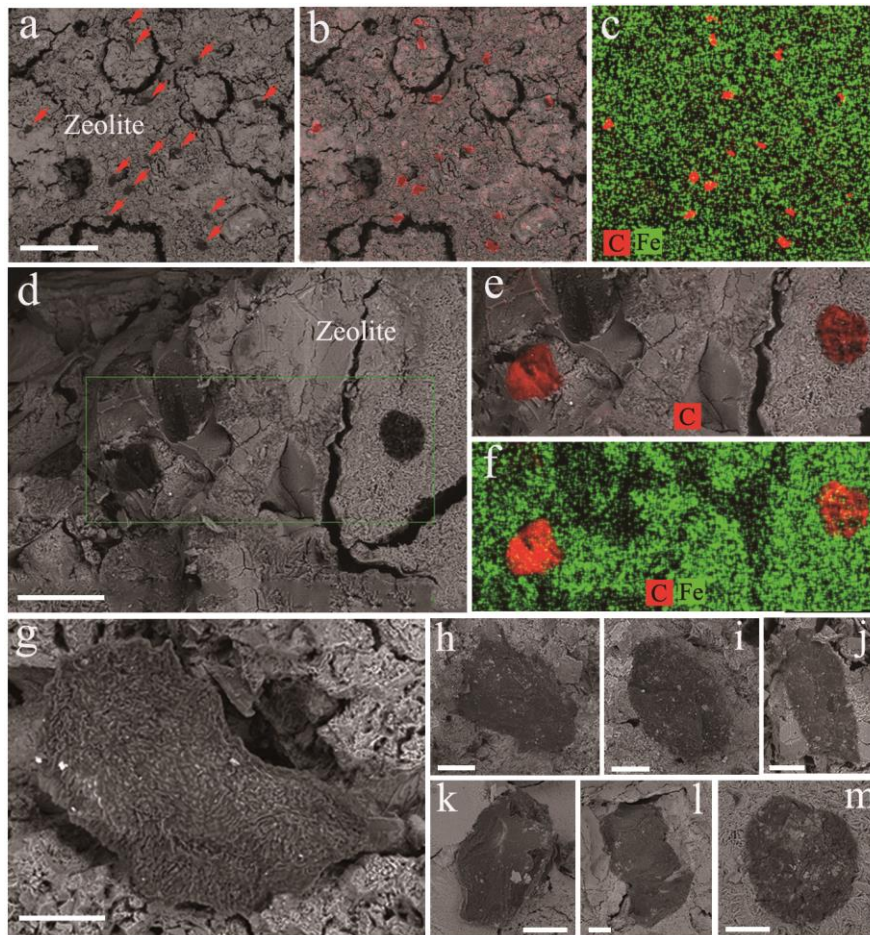


Figure S-3 Representative disordered carbonaceous matter (DCM) embedded in zeolite from the metamorphic ocean crust of the SMT. **(a)** SEM-BSE image showing the distributions of DCM (red arrows) in the zeolite from sample JL119-G02. **(b)** Combined SEM-BSE, shown in panel **a**, and EDS images showing the distribution of carbon in red. **(c)** SEM-EDS mappings (correspond to panel **a**), showing the distribution of carbon in red and iron in green. **(d)** SEM-BSE image showing the distributions of DCM in the zeolite from sample JL120-G02. **(e)** Combined SEM-BSE and EDS images generated from the green box in panel **d**, showing the distribution of carbon in red. **(f)** SEM-EDS map (corresponds to panel **e**), showing the distribution of carbon in red and iron in green. **(g-m)** Enlarged SEM-BSE images of various DCMs in zeolite from sample JL121-G04, showing that they are characterised by compacted patchy organic matter. Scale bars are 200 μm for panel **a**, 40 μm for panel **d**, 10 μm for panels **g-m**.

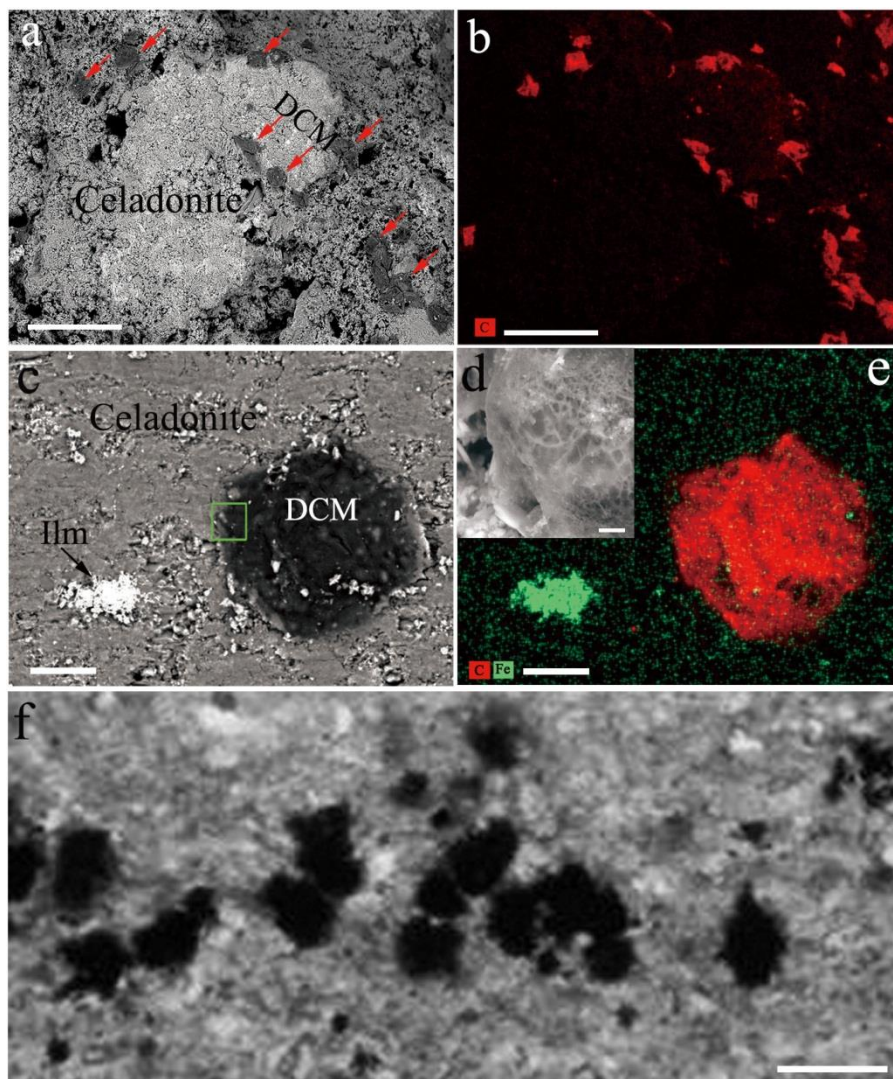


Figure S-4 Representative disordered carbonaceous matter (DCM) embedded in celadonite from the metamorphic ocean crust of the SMT (sample JL122-G02). **(a)** SEM-BSE image showing the distributions of DCM (red arrows) in celadonite. **(b)** SEM-EDS map (corresponds to panel a), showing the distribution of carbon in red. **(c)** SEM-BSE image of DCM in celadonite (Ilm: ilmenite). **(d)** Enlarged SEM-BSE microphotograph generated from the green box in panel c, showing the presence of net-like, loosely or condensed-gel structures within DCM. **(e)** SEM-EDS map (corresponds to panel c), showing the distribution of carbon in red and iron in green. **(f)** Transmitted white light photomicrograph of DCMs in celadonite. Scale bars are 100 μm for panels a, b, f, 10 μm for panels c, e, 1 μm for panel d.

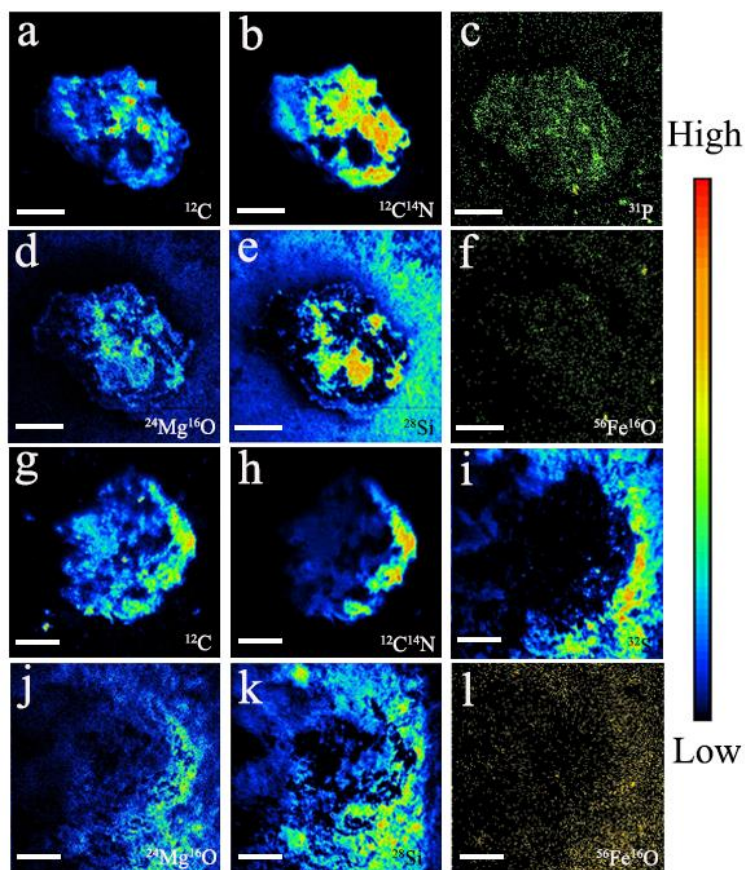


Figure S-5 NanoSIMS element maps of carbonaceous matters in celadonite from sample JL122-G01. **(a-f)** Element images of ^{12}C , $^{12}\text{C}^{14}\text{N}$, ^{31}P , $^{24}\text{Mg}^{16}\text{O}$, ^{28}Si , and $^{56}\text{Fe}^{16}\text{O}$ were generated from a loose, carbonaceous structure with oval morphology. **(g-l)** Element images of ^{12}C , $^{12}\text{C}^{14}\text{N}$, ^{32}S , $^{24}\text{Mg}^{16}\text{O}$, ^{28}Si , and $^{56}\text{Fe}^{16}\text{O}$ were generated from a loose, carbonaceous structure with rounded morphology. Note that the carbonaceous matters are chiefly composed of carbon (C), nitrogen (N) and phosphorus (P) whereas the matrix contains magnesium (Mg), iron (Fe) and silicon (Si). Ion intensity variations are shown by the calibration bar. Scale bars are 10 μm for all panels.

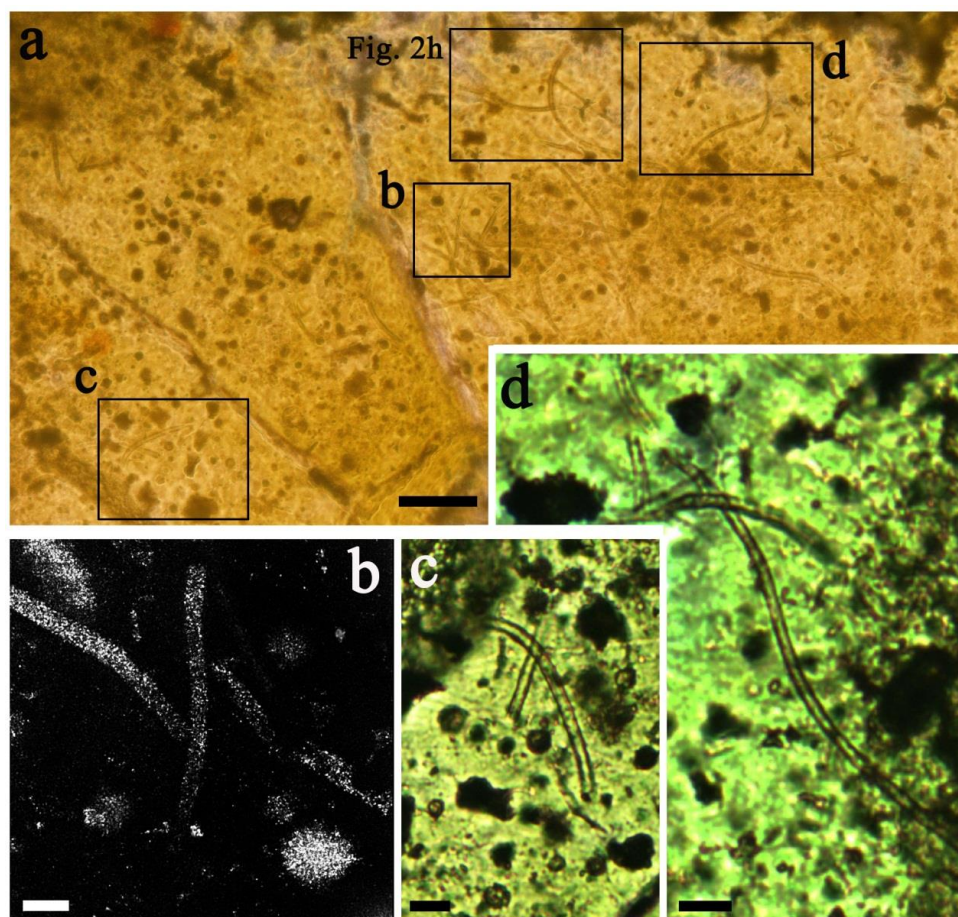


Figure S-6 Filamentous microfossils preserved in the celadonite from the metamorphic ocean crust of the south slope of SMT (sample JL122-G01). **(a)** Transmitted white light image showing the distributions of filamentous microfossils within the celadonite from polished thin section. **(b)** Two-dimensional CLSM image viewed in the plane of the thin section, rotated to an oblique view in Figure 2j. **(c-d)** Enlarged views of microfossils in panel a, showing that they are usually tubular, non-septate, unbranched filaments. The scale bar is 40 μm for panel a, 5 μm for panels b, 10 μm for panels c-d.

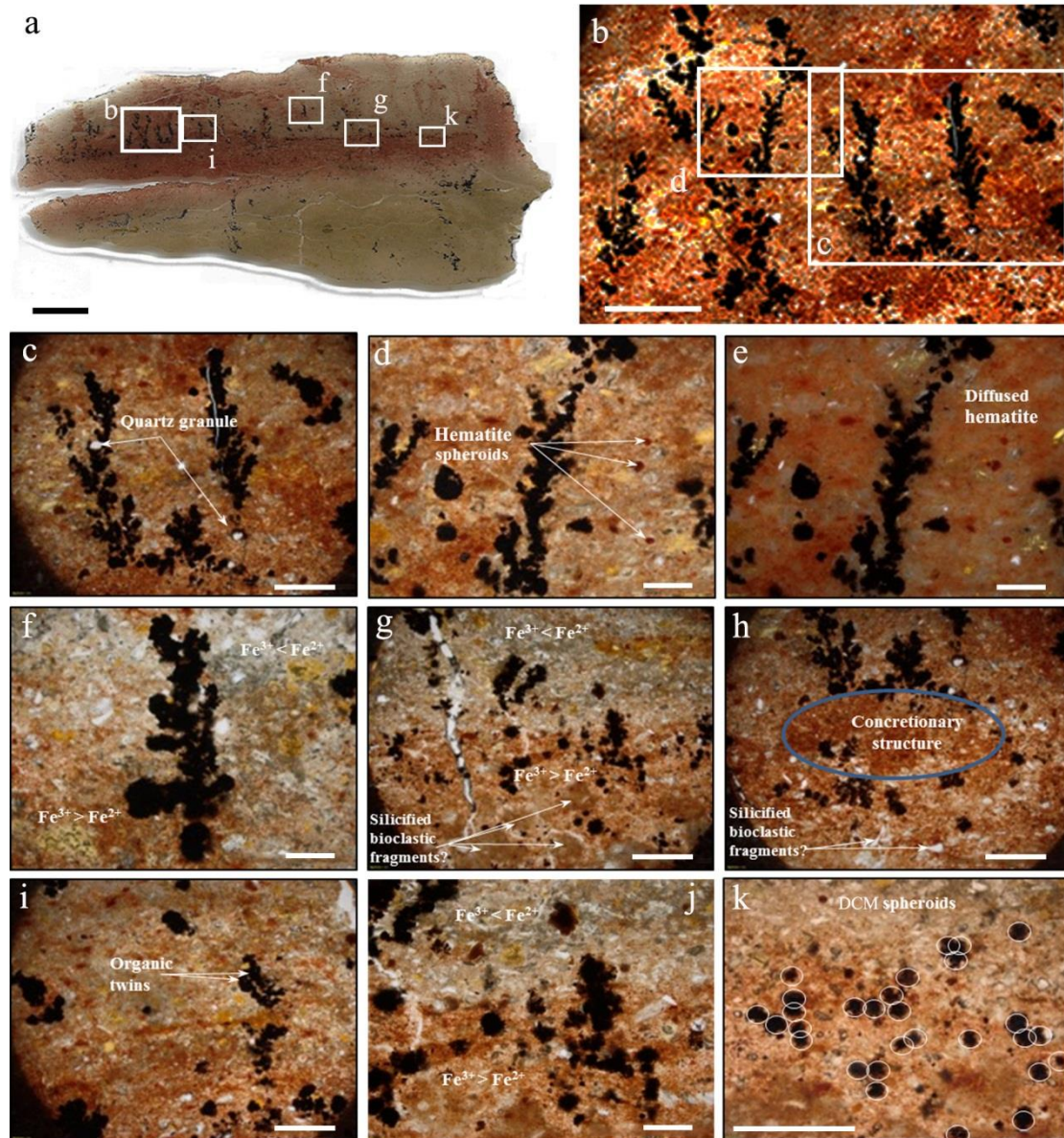


Figure S-7 *Frutexites*-like structures in celadonite from the metamorphic ocean crust of the SMT (sample JL122-G02). **(a)** The thin section showing the fields of b, f, g, i and k (white box). **(b-k)** Transmitted white light photomicrograph of *Frutexites*-like structures associated with disordered carbonaceous matter (DCM) in celadonite. Notably, the *Frutexites*-like structures occur in parts of the green rocks that are more orange to red, qualitatively with higher levels of ferric iron, which suggests that they were involved in Fe oxidation (Heim *et al.*, 2017). The scale bar is 5 mm for panel a, 1 mm for panel b, 500 μm for panels c, g-i, 200 μm for panels d-f, j-k.

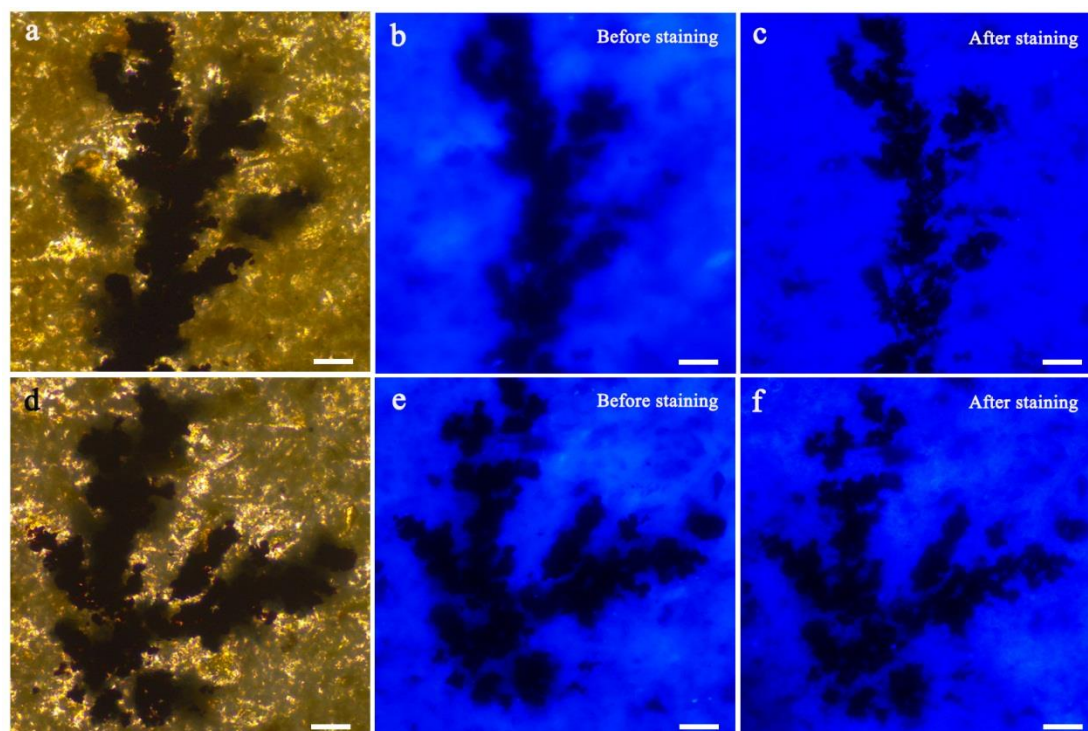


Figure S-8 Photomicrographs of typical *Frutexites*-like structures in the sample JL120-G03. **(a, d)** Transmitted white light photomicrograph of *Frutexites*-like structures. **(b, c)** Same area as **(a)** viewed with an epifluorescence microscopy before and after staining with DAPI, respectively. **(e, f)** Same area as **(d)** viewed with an epifluorescence microscopy before and after staining with DAPI, respectively. Note that no DNA was detected by DAPI in the samples, showing that DNA has been degraded and these structures may result from past growth of microorganisms. Scale bars are 50 μm for all panels.

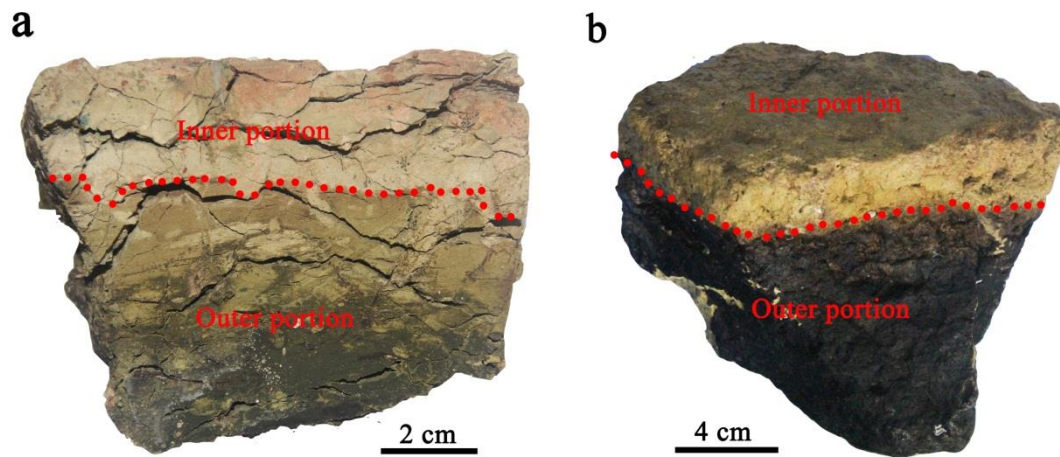


Figure S-9 The sampling sites for the inner and outer portions of metamorphic rocks selected for the lipid analysis. **(a)** The sample JL122-G02. **(b)** The sample JL121-G04.

Supplementary Video

Video S-1 Tubular filaments revealing the existence of a “hollow” lumina.

Video S-1 is available for download from the online version of this article at <https://www.geochemicalperspectivesletters.org/article2017>.

Supplementary Information References

- Alt, J.C., Muehlenbachs, K., Honnorez, J. (1986) An oxygen isotopic profile through the upper kilometer of the oceanic crust, DSDP Hole 504B. *Earth and Planetary Science Letters* 80, 217-229.
- Fang, J., Findlay, R.H. (1996) The use of a classic lipid extraction method for simultaneous recovery of organic pollutants and microbial lipids from sediments. *Journal of Microbiological Methods* 27, 63-71.
- Fang, J., Lyon, D.Y., Wiesner, M.R., Dong, J., Alvarez, P.J.J. (2007) Effect of a Fullerene Water Suspension on Bacterial Phospholipids and Membrane Phase Behavior. *Environmental Science and Technology* 41, 2636-2642.
- Fisk, M. R., Popa, R., Mason, O.U., Storrie-Lombardi, M.C., Vicenzi, E.P. (2006) *Astrobiology* 6, 48-68.
- Guo, Z., Peng, X., Czaja, A.D., Chen, S., Ta, K. (2018) Cellular taphonomy of well-preserved Gaoyuzhuang microfossils: A window into the preservation of ancient cyanobacteria. *Precambrian Research* 304, 88-98.
- Hall, A. (1993) Application of the indophenol blue method to the determination of ammonium in silicate rocks and minerals. *Applied Geochemistry* 8, 101-105.
- Hopmans, E.C. et al. (2004) A novel proxy for terrestrial organic matter in sediments based on branched and isoprenoid tetraether lipids. *Earth and Planetary Science Letters* 224, 107-116.
- Papineau, D., She, Z., Dodd, M.S. (2017) Chemically-oscillating reactions during the diagenetic oxidation of organic matter and in the formation of granules in late Palaeoproterozoic chert from Lake Superior. *Chemical Geology* 470, 33-54.
- Peng, X., Guo, Z., House, C.H., Chen, S., Ta, K. (2016) SIMS and NanoSIMS analyses of well-preserved microfossils imply oxygen-producing photosynthesis in the Mesoproterozoic anoxic ocean. *Chemical Geology* 441, 24-34.
- Schouten, S., Hopmans, E.C., Sinninghe Damsté, J.S. (2013) The organic geochemistry of glycerol dialkyl glycerol tetraether lipids: a review. *Organic Geochemistry* 54, 19-61.
- Sturt, H.F., Summons, R.E., Smith, K., Elvert, M., Hinrichs, K.U. (2004) Intact polar membrane lipids in prokaryotes and sediments deciphered by high performance liquid chromatography/electrospray ionisation multistage mass spectrometry-new biomarkers for biogeochemistry and microbial ecology. *Rapid Communications in Mass Spectrometry* 18, 617-628.
- Weijers, J.W.H., Schefu, E., Kim, J.H., Sinninghe Damsté, J.S., Schouten, S. (2014) Constraints on the sources of branched tetraether membrane lipids in distal marine sediments. *Organic Geochemistry* 72, 14-22.
- Winter, J.D. (2010) Principles of Igneous and Metamorphic Petrology. Second Edition, Prentice Hall, New Jersey, 541-548.
- Xie, W., Zhang, C.L., Ma, C.L. (2015) Temporal variation in community structure and lipid composition of Thaumarchaeota from subtropical soil: Insight into proposing a new soil pH proxy. *Organic Geochemistry* 83-84, 54-64.
- Xu, H., Chen, T., Konishi, H. (2010) HRTEM investigation of trilling todorokite and nano-phase Mn-oxides in manganese dendrites. *American Mineralogist* 95, 556-562.

